Current redistribution and generation of kinetic energy in the stagnated *Z* pinch

V. V. Ivanov,* A. A. Anderson, D. Papp, A. L. Astanovitskiy, and B. R. Talbot
Department of Physics, University of Nevada, Reno, Nevada 89557, USA

J. P. Chittenden and N. Niasse
Blackett Laboratory, Imperial College, London SW7 2BZ, United Kingdom

(Received 12 April 2013; revised manuscript received 3 July 2013; published 31 July 2013)

The structure of magnetic fields was investigated in stagnated wire-array *Z* pinches using a Faraday rotation diagnostic at the wavelength of 266 nm. The distribution of current in the pinch and trailing material was reconstructed. A significant part of current can switch from the main pinch to the trailing plasma preheated by x-ray radiation of the pinch. Secondary implosions of trailing plasma generate kinetic energy and provide enhanced heating and radiation of plasma at stagnation. Hot spots in wire-array *Z* pinches also provide enhanced radiation of the *Z* pinch. A collapse of a single hot spot radiates 1%–3% of x-ray energy of the *Z* pinch with a total contribution of hot spots of 10%–30%.

DOI: 10.1103/PhysRevE.88.013108 PACS number(s): 52.58.Lq, 52.59.Qy, 52.70.Kz, 52.70.La

I. INTRODUCTION

Since the 1950s, wide studies of *Z* pinches have been initiated in connection with investigations on controlled fusion [1]. Further interest in dense *Z* pinches was supported by the development of fast pulsed-power generators and new conceptions for *Z* pinches. At the present time, wire-array and gas-puff *Z* pinches generate record power and energy of soft and keV x-ray radiation with wall-plug efficiency $>15\%$ [2–5]. Powerful *Z* pinches are used in fusion research, atomic and radiation physics, and laboratory astrophysics [1,6]. However, the sophisticated physics of the dense *Z* pinch is still not well understood in some aspects. *Z*-pinch plasma is unstable for magnetohydrodynamics (MHD) instabilities and is subjected to the magneto-Rayleigh-Taylor instability during implosion [1,7]. Simulations and ultraviolet (UV) laser probing show a complicated structure of the pinch with fast plasma motion at stagnation [8–10]. Instabilities and other effects in the *Z* pinch can generate enhanced radiation compared to available kinetic energy and Spritzer heating of plasma [11–13]. Several mechanisms have been suggested to explain this effect, including the resistive effect in Hall plasma [14], dissipation of magnetic flux [15–17], interchange ion viscous heating [18], and expansion of the $m = 1$ helix [19]. The mechanisms of the enhanced plasma heating have not been identified in experiments. Plasma instability also results in the formation of bright and hot x-ray spots on the *Z* pinch, which produce a significant part of *Z*-pinch radiation. Bright spots in pinches are sources of high-temperature and high-density plasma [9,13,20–23].

Parameters of plasma in the *Z* pinch and hot spots strongly depend on the distribution and evolution of current in the pinch and trailing material. Knowing the current distribution is crucial for physics of the *Z* pinch, but it is difficult to measure with regular apparatus. Faraday rotation diagnostics at the optical wavelengths can be applied only to the precursor [24] and low-density plasma near the stagnated pinch [25,26]. Using Faraday rotation diagnostics at 532 nm, the authors of Ref. [25] reported a "disappearance" of current in the neck of the fiber *Z* pinch. Authors of a later paper [26] reported that 70% of total current flows in the fiber *Z*-pinch neck. Redistribution of current to the external plasma was theoretically studied in Refs. [27,28]. Three-dimensional (3D) MHD Gorgon simulations showed that only a quarter of the total current flows in the dense pinch in some configurations of wire arrays [9]. Anyway, the structure of current inside the pinch and trailing plasma has never been reconstructed in experiments.

UV laser diagnostics can deliver data about the internal structure, plasma density, and mega-Gauss (MG) magnetic fields in the stagnated *Z* pinch.

In this paper we directly study a structure of sub-MG magnetic fields and reconstruct a distribution of current in the stagnated wire-array *Z* pinches using a Faraday rotation diagnostic at the wavelength of 266 nm. A significant part of current can switch from the main pinch to the trailing plasma, preheated by x-ray radiation of the main pinch if the inductance of the pinch rises due to sausage and kink instabilities. Configuration of plasma with split or widely distributed current is typical for observed 1 MA *Z* pinches. Secondary implosions of current-carrying trailing plasma provide additional kinetic energy. Thermalization of kinetic energy provides enhanced radiation of *Z* pinches. Another source of kinetic energy at stagnation is the collapse of hot spots in the *Z* pinch. An analysis of x-ray streak images shows that hot spots generate 10%–30% of the total radiation energy of small-diameter and planar wire-array *Z* pinches.

II. EXPERIMENTAL SETUP

The experiments were carried out at the 1 MA Zebra generator with a rising edge of the current pulse of 80 ns and an impedance of 1.9 Ω. X-ray diagnostics included a streak camera, six-frame pinhole camera, time-integrating spectrometer with a convex potassium acid phthalate crystal, filtered x-ray diodes, photoconducting detectors (PCDs), and bare Ni and Au bolometers. The streak camera with Au and CsI photocathodes and 80 μm slit was used at a 50 ns sweep range with 100 ps resolution. Another slit was used to build a one-dimensional (1D) image of the pinch on the slit of

*Corresponding author: ivanov@physics.unr.edu

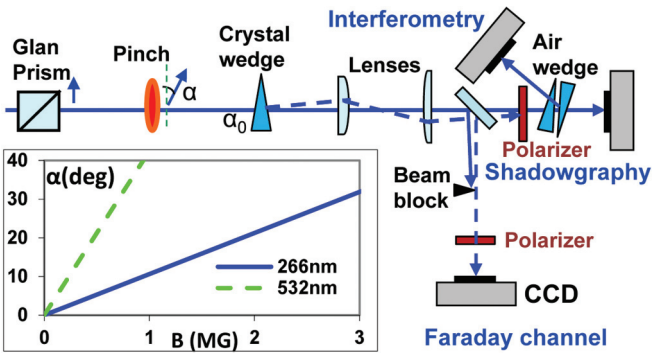

FIG. 1. (Color online) The simplified optical schematic of the three-channel polarimeter. The diagram compares rotation angles of the polarization plane of the laser beam at 532 and 266 nm in a plasma slab with the electron density of 10^{20} cm^{-3} and length of 1 mm.

the streak camera. The time-gated pinhole camera provided two sets of images at ranges of $E_1 > 0.8$ and $E_2 > 3$ keV with the frame duration of 3 ns. Laser diagnostics of plasma included one probing direction for UV diagnostics at 266 nm and two directions for four-frame shadowgraphy at 532 nm. UV diagnostics can operate as two-frame shadowgraphy and interferometry or a Faraday rotation three-channel polarimeter with the Faraday rotation, shadowgraphy, and differential interferometry channels [24,29]. Two commercial lasers at wavelengths of 532 and 266 nm provided probing pulses with durations of 150 ps. All channels of shadowgraphy, interferometry, and Faraday diagnostics were co-aligned using the tip of a needle in the center of the wire array.

An optical schematic of the three-channel polarimeter for Faraday rotation measurements is presented in Fig. 1. The regular optical schematic of the Faraday diagnostic [24] is modified for the UV range. The first polarizer provides linear polarization of the laser beam with a contrast $>10^5$. The crystal wedge after plasma is used as an analyzer for the rotation angle. Depolarized light is shown by the dashed line. The analyzer is not crossed with the first polarizer but is mismatched with angle α_0. This creates a background illumination of the charge-coupled device (CCD) in the Faraday channel and allows identification of the direction of magnetic fields. The Faraday beam is separated from the shadowgraphy channel by the knife edges placed in the lens focuses. A field of view of the Faraday diagnostic is 8×8 mm^2 with spatial resolution of 15 μm. The rotation angles of the polarization plane of laser beams at wavelengths of 532 and 266 nm are compared in the plasma slab with the electron density of 10^{20} cm^{-3} and length of 1 mm as shown in the diagram in Fig. 1. The rotation angle is too large at 532 nm, $\alpha > 20^\circ$ for the magnetic field $B < 0.5$ MG, but it is in the optimal range for the UV diagnostic if $B = 0.2$–2 MG. The maximum magnetic field measurable at 266 nm may be higher in small plasma objects. The experiments were carried out with 2 cm tall Al (alloy 5056) and Ni cylindrical wire arrays 3–16 mm in diameter.

III. MEASUREMENTS OF MAGNETIC FIELDS IN THE *Z* PINCH

Due to the complicated structure of the stagnated *Z* pinch, Faraday images should be interpreted and processed to derive the quantitative data about the magnetic field and current. Figure 2 presents calculations of the rotation angle α of the polarization plane of the probing beam in plasma in several configurations of *Z*-pinch plasma. A current density was calculated for cylindrical symmetry.

A solid curve in Fig. 2(a) shows a rotation angle α in the plasma column with radius $R_0 = 0.5$ mm, total current $I_0 = 1$ MA, and both constant distributions for the electron plasma density $N_0 = 10^{20}$ cm^{-3} and density of current $j_c = I_0/\pi R_0^2$. A dashed curve is calculated with both parabolic distributions of the electron plasma density and density of current. Profiles

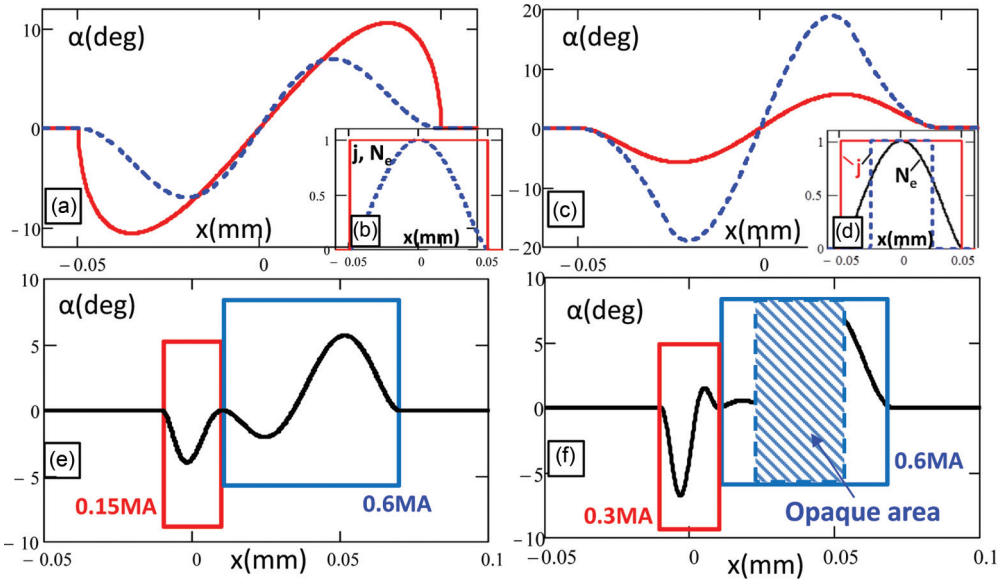

FIG. 2. (Color online) The angle of rotation of the polarization plane of the probing laser beam calculated for (a) and (c) single current-carrying plasma columns and (e) and (f) two closely located plasma columns. Diagrams (b) and (d) show the profiles for the plasma and current densities.

of appropriate constant and parabolic distributions are shown in diagram (b). The peak rotation angles are higher at the constant distributions of parameters in the solid curve compared to parabolic distributions of the plasma and current densities in the dashed curve.

Figure 2(b) compares rotation angles in single plasma columns with the parabolic distribution for $N_e(r)$ and constant current density $I_0 = 0.6$ MA. The radii of current-carrying cylinders are $R_1 = 0.5$ mm in a solid curve and $R_2 = 0.25$ mm in a dashed curve. The profiles for plasma and current densities are presented in Fig. 2(d). The peak magnetic field and rotation angle are significantly higher if current does not flow in the peripheral areas of the plasma column but is contained in the small-diameter channel.

Figures 2(e) and 2(f) show the rotation angles in two closely located plasma columns with the constant electron density $N_0 = 10^{20}$ cm^{-3}, parabolic current density $j(r)$, radii of columns of $R_1 = 0.1$ and $R_2 = 0.3$ mm, and total currents in two plasma columns of (e) 0.15/0.6 MA and (f) 0.3/0.6 MA. The shaded rectangle in Fig. 2(f) presents a suggested opaque area in the Z pinch. Two current-carrying plasma columns create specific configurations of magnetic fields and rotation angles α. A typical picture of rotation angles in image (f) shows the positive angles on both sides of the dense opaque pinch and the negative rotation angle on the left side of the left plasma column. Positive and negative rotation angles in simulations are seen as lightening and darkening in the Faraday image. This simple analysis helps to interpret experimental Faraday images.

Figure 3 shows shadowgrams and complementary Faraday images at the wavelength of 266 nm from two shots with Al cylindrical wire arrays 8 mm in diameter. Faraday image (b) demonstrates general lightening in the right side and darkening

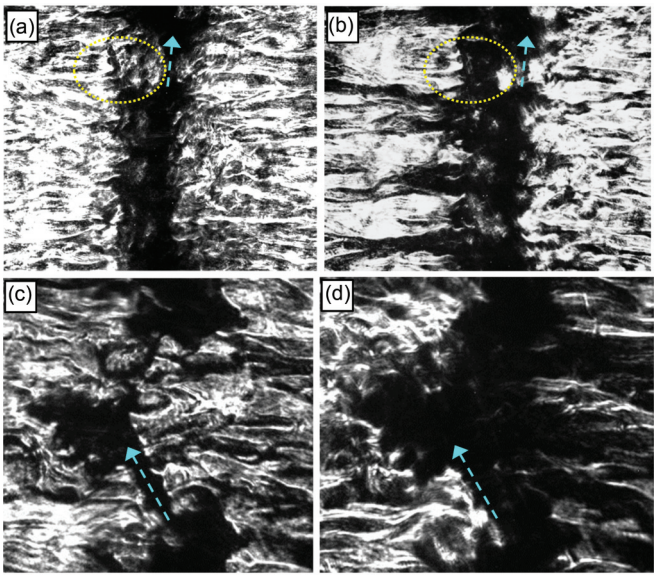

FIG. 3. (Color online) (a) and (c) Shadowgrams and (b) and (d) complementary Faraday images from two shots with Al cylindrical loads, 8 mm in diameter, $m = 54$ μg. Images (a) and (b) from shot 2936 are timed 2 ns before the maximum of the x-ray pulse, the mismatch angle is $\alpha_0 = +7.6^\circ$. Images (c) and (d) from shot 2678 are timed to the maximum of the x-ray pulse $\alpha_0 = -5.5^\circ$.

of plasma "fingers" on the left side of the image due to the opposite directions of magnetic fields. The dashed arrow shows the position of the dense neck in both (a) shadowgram and (b) Faraday image. The dashed circles on the left of the arrows show the difference in the Faraday image compared to the shadowgram. There is an additional dark area in the Faraday image separated from the dense neck by the lightened area. The configuration of the rotation angles in the Faraday image qualitatively correlates with a model of current split in two plasma columns as seen in Fig. 2(f).

Areas of darkening and lightening are inverted in Fig. 3(d) compared to the Faraday image in Fig. 3(b) due to the negative mismatch angle α_0 that was installed in this shot. Rotation angles α in Faraday images were calculated using the shadowgram, Faraday image, and their reference images taken before the Z-pinch shot. The bias of the CCD camera and intensity of plasma self-radiation were subtracted from the intensity of the laser beam. Typical angles of rotation of the polarization plane in the pinch and trailing plasma are in the range of $\alpha = 2^\circ$–6°. Small rotation angles show that current is not contained in the narrow pinch shown by the arrow in shadowgram Fig. 3(c) but is distributed in a wide area of trailing plasma with the radial size >2 mm.

Figure 4 presents calculations of the electron density, magnetic field strength, and current in the trailing plasma from the shot with Al cylindrical eight-wire array 16 mm in diameter. Figure 4 displays (a) shadowgram, (b) Faraday image, and (c) interferogram of the central area of the pinch at the maximum of the radiated x-ray pulse. Processing of data from Faraday diagnostics includes several steps. First, a phase shift is calculated from the differential interferogram. The profile of the electron density is reconstructed with the Abel transform [30],

$$N_e(r) = -K \int_r^{R_0} \frac{d\varphi(y)}{dy} \frac{dy}{\sqrt{y^2 - r^2}}, \qquad (1)$$

where $\varphi(y)$ is the phase shift, y is the distance from the axis, R_0 is the plasma column radius, $K = 2e^2\lambda/mc^2$) in Gaussian units, λ is the wavelength, e and m are the charge and mass of an electron, and c is the speed of light. The rotation angle of the polarization plane is calculated from (b) Faraday image, (a) shadowgram, and their reference images as described in Ref. [24]. The rotation angle diagram in Fig. 4(e) includes the area of darkening and two zones of lightening near the opaque plasma pinch and correlates with the diagram in Fig. 2(f) calculated for two current-carrying plasma columns. Due to possible error, areas of lightening close to the dense pinch were not used for calculations of magnetic fields. The magnetic field in the dashed circle in the Faraday image was calculated using the Abel transform,

$$\frac{B(r)N_e(r)}{r} = -\frac{2}{\pi\kappa} \int_y^{R_0} \frac{d}{dy}\left(\frac{\beta(y)}{y}\right) \frac{dy}{\sqrt{y^2 - r^2}}, \qquad (2)$$

where β is the rotation angle and $\kappa = 2e^3\lambda^2/(\pi m^2 c^4)$ in Gaussian units. The electron density $N_e(r)$ from Fig. 4(d) was used for the calculation of $B(r)$ with formula (2). The reconstructed magnetic field is presented in Fig. 4(f). The maximum strength of the magnetic field in the area of darkening exceeds 0.4 MG. This magnetic field was modeled

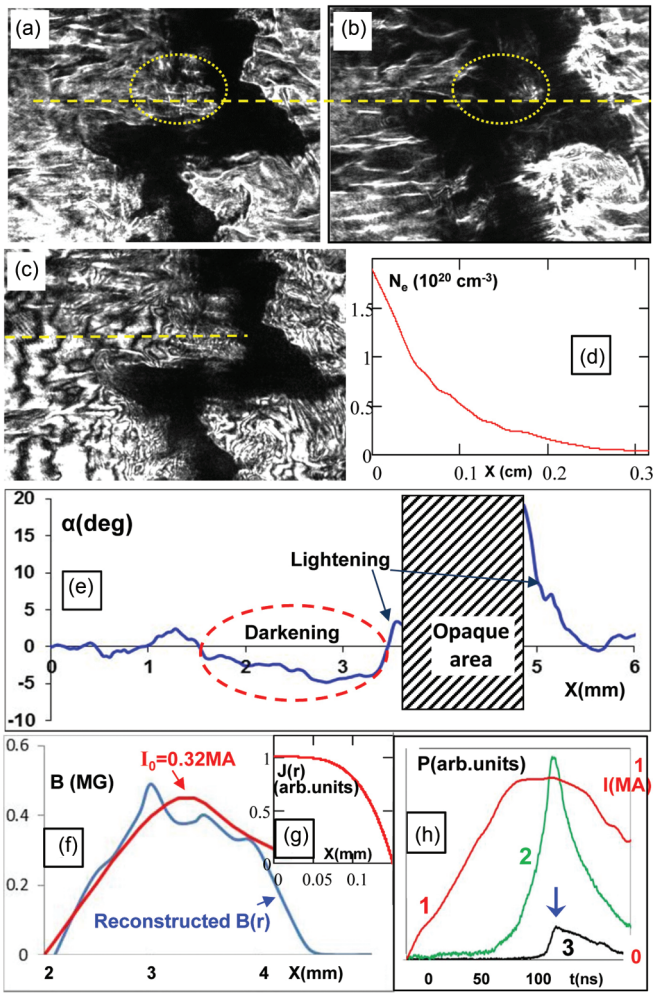

FIG. 4. (Color online) (a) Shadowgram, (b) Faraday image, and (c) interferogram of the pinch from implosion of the Al cylindrical wire array 16 mm in diameter with eight 15 μm wires, shot 2672. The mismatch angle in the Faraday image is $\alpha_0 = +5.7^\circ$. (e) The rotation angle calculated along the dashed line in images (a)–(c) starting from the edge. (d) The plasma electron density $N_e(r)$ reconstructed starting from the edge of the opaque pinch. (f) The reconstructed magnetic fields at the area of darkening in image (e) and the magnetic field calculated with a parabolic current density profile shown in diagram (g). (h) The timing diagram for the current pulse (1), total x-ray pulse (2), keV x-ray pulse (3), and UV frames (arrow).

for current with parabolic distribution as shown in diagram (g). The magnetic field calculated for current $I = 0.32$ MA fits the magnetic field reconstructed in the circle area in Fig. 4(b). The estimated accuracy of this calculation is $\pm 40\%$. The main source of errors is linked to simulations of plasma density and magnetic field using a model with cylindrical symmetry. Cylindrical symmetry allows the reconstruction of profiles for $N_e(r)$ and $B(r)$, but it may deviate from the more complicated real distribution. In any case, simulations show that a significant part of the total 1 MA current switches to the channel in trailing material. Some current is also flowing in the wide low density plasma seen in shadowgrams and interferograms. We suggest that redistribution of current is driven by the increase in the pinch inductance due to micropinching or kink instability. Trailing plasma is initially cold and has high resistivity compared to the pinch plasma, but we suggest that it can be heated by radiation of the pinch. In Ref. [9], it was calculated that an x-ray burst from the pinch can significantly increase the temperature and drop the resistance of nonimploded and trailing plasma. Current distributed at the radius of 2 to 3 mm implodes and provides the enhanced heating of the pinch plasma. Two mechanisms are involved for the enhanced heating. First, the later implosion of the nonimploded plasma provides additional energy deposition into the radiating plasma column [9,31]. The nonimploded plasma is heated by x-ray radiation of the main pinch [9] and accepts part of the main current of the Z pinch. The secondary implosion also helps to confine the pinch during 20–25 ns. Second, implosions of trailing mass at stagnation generate additional kinetic energy in the pinch. The kinetic energy of the imploding plasma at stagnation can be estimated as a change in the pinch inductance [15]. If the radius of the plasma column changes from 3 to 0.7 mm at a current of 0.3 MA, then the kinetic energy of implosion is 0.6 kJ. Two-frame UV diagnostics show that the characteristic time for the pinch plasma motion is 35 ns [9]. This means power of 0.12–0.2 TW can be generated by these plasma oscillations that is 20%–30% of power radiated by the typical 3 mm cylindrical wire array [13].

IV. SIMULATIONS OF THE ENERGY BALANCE IN THE Z PINCH

Simulations of the total energy and power balance were performed with the 3D MHD Gorgon program, using techniques similar to those of Ref. [32]. Here we model a 2 cm long, 8 mm diameter, array composed of eight 15 μm aluminum wires. By calculating the average axial electric field across the pinch (at a radius of 9 mm from the array axis) we can monitor the Poynting flux delivered to the pinch by the generator. Figure 5(a) shows that this provides the primary source of all energy within this radius and is equal to the volume integral of the thermal, kinetic, and magnetic energies plus the energy lost to radiation. The maximum instantaneous kinetic energy in the plasma is 1.03 kJ, which is significantly less than the x-ray yield, but this does not provide an accurate estimate for the energy coupled to the plasma. Figure 5(b) shows that the mechanical work performed by the magnetic field increases the reservoir of kinetic energy prior to stagnation. This kinetic energy resides in a nonuniform imploding plasma shell of $\sim$1 mm width, and thus, there is a $\sim$5 ns delay between the leading edge and the trailing edge of this shell reaching the axis, which roughly corresponds to the x-ray pulse rise time. During this phase the kinetic energy of the leading edge is being dissipated, while at the same time, the trailing edge is still being accelerated, so the total kinetic energy does not drop instantaneously. At 0 ns the pinch has reached peak x-ray emission. The source of energy for emission comes not just from the falling kinetic energy, but also from the mechanical work being performed by the magnetic field $\mathbf{v} \cdot (\mathbf{j} \times \mathbf{B})$, which continues to accelerate and to compress the plasma throughout the poststagnation phase, generating large amplitude 3D MHD instabilities. Note that the plasma motion remains significant even after stagnation. This energy, in turn, comes from the Poynting flux, which sustains the

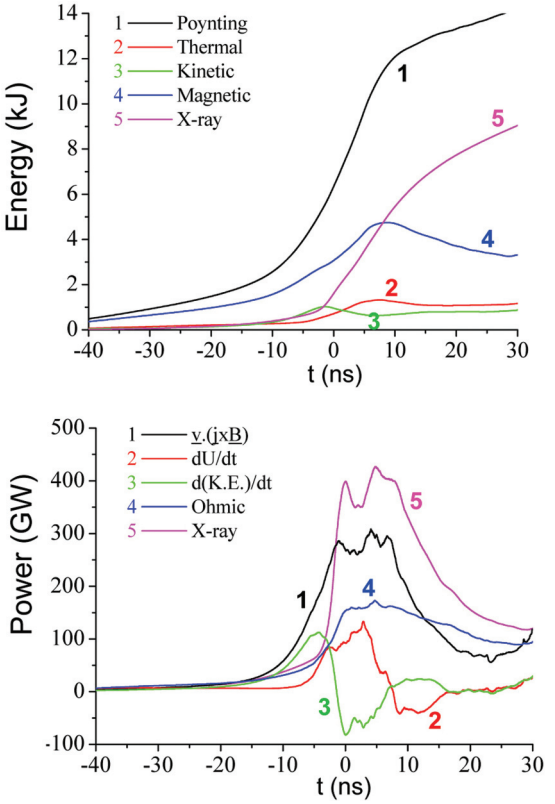

FIG. 5. (Color online) A 3D MHD simulation of the Al cylindrical wire array 8 mm in diameter with eight 15 μm wires, shows (a) that the integral of the Poynting flux delivered to the pinch provides the energy for the sum of the thermal, kinetic, and magnetic energies plus the x-ray yield and (b) that the power required to heat the plasma and to emit x rays is provided by the mechanical work performed by the magnetic field $\mathbf{v} \cdot (\mathbf{j} \times \mathbf{B})$, the Ohmic heating, and the dissipation of kinetic energy (K.E.).

strength of the magnetic energy reservoir surrounding the pinch, despite the increasing inductance. Throughout the x-ray pulse, including the poststagnation phase, the x-ray power emitted and the rate of thermal energy gain in the plasma are balanced by the volume integral of the $\mathbf{v} \cdot (\mathbf{j} \times \mathbf{B})$ term, the Ohmic heating, and the dissipation of kinetic energy.

V. HOT SPOTS IN THE *Z* PINCH

Hot spots in *Z*-pinch plasma also can generate enhanced x-ray radiation [11,12,33]. The extreme plasma conditions were measured in the *X*-pinch hot spot with the electron density $N_e > 10^{22}$ cm^{-3} and temperature of 1–9 keV [22,23]. MHD simulations predict peak density >400 g/cm^3 in the *X* pinch [23]. We investigated dynamics and energy deposition of hot spots in wire-array *Z* pinches with temporal and 1D spatial resolution using the x-ray streak camera. Figure 6 presents (a) nonfiltered and (c) filtered by 7.5 μm Kapton film streak images of wire arrays 3 mm in diameter. Small-diameter wire arrays generate *Z* pinches with numerous bright spots [13]. Figure 6(a) shows that power of bright spots is much higher than radiation of bulk *Z*-pinch plasma. UV shadowgrams show formation of long-lasting necks on the pinch [9]. There is a strong difference between regular necks and hot spots. Necks

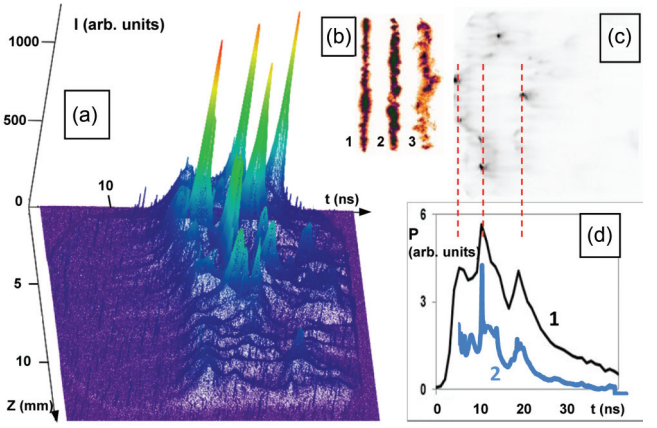

FIG. 6. (Color online) (a) A 3D plot of the streak image of implosion of the Ni eight-wire array 3 mm in diameter, $m = 60$ μg, shot 2960 recorded with the Au cathode and a 64 μm imaging slit without filters. (b) Three x-ray frames with durations of 3 ns filtered by 15 μm Be foil taken from shot 2960. (c) The streak image from implosion of the Al eight-wire array 3 mm, in diameter, $m = 74$ μg, shot 3053 recorded with the CsI cathode through the 38 μm imaging slit and filtered by a 7.5 μm Kapton film. (d) The wave form from PCD filtered by 8 μm Be foil (1) and spatially integrated plot (2) from the streak image (c).

can exist >10 ns. Radiation of necks is seen in a 3D streak image, Fig. 6(a), as ridges on background radiation. True hot spots are presented on the streak image as short peaks with high intensity increased by a factor of 10–30 compared to the background. The hot spot lifetime is 0.7–1.5 ns in nonfiltered streak images. Typical sizes of hot spots measured with axial resolution of 0.15 mm are in the range of 0.3–0.6 mm. Hot spots radiate wide continuum in x-ray spectra similar to bremsstrahlung radiation. Calculations of energy of hot spots from streak images show that a single hot spot can radiate 1% to 2% of x-ray energy of the small-diameter wire arrays with a total contribution from hot spots of 10%–30%.

Radiation of hot spots in the keV range filtered by a 7.5 μm Kapton film is shown in Fig. 6(c). Positions of hot spots in streak image (c) correlate with peaks on the keV PCD wave form but show the shorter bursts. In the keV range, one hot spot can deposit >50% to the power of the *Z* pinch. The contribution of hot spots is the most pronounced in the small-diameter and planar wire arrays.

VI. CONCLUSIONS

The UV Faraday rotation diagnostic unfolds the internal distribution of magnetic fields and allows the reconstruction of current in the *Z* pinch. Current can switch from necks on the main pinch to trailing material due to rising of inductance. Current redistribution impacts the plasma dynamics and radiative properties of the *Z* pinch. The secondary implosions generate additional kinetic energy and enhanced radiation of *Z* pinches. Hot spots also contribute to radiation of the *Z* pinch and can produce 10%–30% of total energy in some types of loads. Secondary implosions and hot spots can explain enhanced radiation of *Z* pinches in soft and keV ranges. However, we do not exclude the effect of other mechanisms

of enhanced plasma heating in the Z pinch. The stagnation stage in Z pinches is a complicated dynamic process with multiple internal implosions and collapses of micropinches. Three-dimensional MHD simulations examining the energy and power balance of the plasma reveal that the x-ray yield can be significantly higher than that anticipated from the convergence of the implosion and is due to significant levels of mechanical work performed by the magnetic field during the MHD unstable poststagnation phase.

ACKNOWLEDGMENTS

The authors thank G. E. Sarkisov, S. V. Lebedev, S. A. Pikuz, and T. A. Shelkovenko for discussions and S. D. Altemera, O. Dmitriev, V. Davis, V. Nalajala, and D. Macauly for help with the experiments. This work was supported by DOE/NNSA under Grant No. DE-SC0008824 and partly under the UNR Grants No. DE-FC52-06NA27616 and No. DE-NA 0002075.

[1] D. D. Ryutov, M. S. Derzon, and M. K. Matzen, Rev. Mod. Phys. **72**, 167 (2000).
[2] R. B. Spielman *et al.*, Phys. Plasmas **5**, 2105 (1998).
[3] C. Deeney, M. R. Douglas, R. B. Spielman, T. J. Nash, D. L. Peterson, P. L'Eplattenier, G. A. Chandler, J. F. Seamen, and K. W. Struve, Phys. Rev. Lett. **81**, 4883 (1998).
[4] W. A. Stygar *et al.*, Phys. Rev. E **69**, 046403 (2004).
[5] M. E. Cuneo *et al.*, Phys. Rev. E **71**, 046406 (2005).
[6] M. K. Matzen *et al.*, Phys. Plasmas **12**, 055503 (2005).
[7] J. P. Friedberg, Rev. Mod. Phys. **54**, 801 (1982).
[8] V. V. Ivanov, J. P. Chittenden, S. D. Altemara, N. Niasse, P. Hakel, R. C. Mancini, D. Papp, and A. A. Anderson, Phys. Rev. Lett. **107**, 165002 (2011).
[9] V. V. Ivanov, J. P. Chittenden, R. C. Mancini, D. Papp, N. Niasse, S. D. Altemara, and A. A. Anderson, Phys. Rev. E **86**, 046403 (2012).
[10] S. A. Pikuz, J. D. Douglass, T. A. Shelkovenko, D. B. Sinars, and D. A. Hammer, Rev. Sci. Instrum. **79**, 013106 (2008).
[11] C. Deeney, T. Nash, R. R. Prasad, L. Warren, K. G. Whitney, J. W. Thornhill, and M. C. Coulter, Phys. Rev. A **44**, 6762 (1991).
[12] D. B. Sinars, R. W. Lemke, M. E. Cuneo, S. V. Lebedev, E. M. Waisman, W. A. Stygar, B. Jones, M. C. Jones, E. P. Yu, J. L. Porter, and D. F. Wenger, Phys. Rev. Lett. **100**, 145002 (2008).
[13] V. V. Ivanov, V. I. Sotnikov, J. M. Kindel, P. Hakel, R. C. Mancini, A. L. Astanovitskiy, A. Haboub, S. D. Altemara, A. P. Shevelko, E. D. Kazakov, and P. V. Sasorov, Phys. Rev. E **79**, 056404 (2009).
[14] V. L. Kantsyrev, L. I. Rudakov, A. S. Safronova, D. A. Fedin, V. V. Ivanov, A. L. Velikovich, A. Esaulov, A. S. Chuvatin, K. Williamson, N. D. Quart, V. Nalajala, G. Osborne, I. Shrestha, M. F. Yilmatz, S. Pokala, P. J. Laca, and T. E. Cowan, IEEE Trans. Plasma Sci. **34**, 2295 (2006).
[15] A. I. Velikovich, J. Davis, J. W. Thornhill, J. L. Giuliani, Jr., L. I. Rudakov, and C. Deeney, Phys. Plasmas **7**, 3265 (2000).
[16] R. Riley, D. Scudder, J. Shlachter, and R. Lovberg, Phys. Plasmas **3**, 1314 (1996).
[17] L. I. Rudakov, A. L. Velikovich, J. Davis, J. W. Thornhill, J. L. Giuliani, and C. Deeney, Phys. Rev. Lett. **84**, 3326 (2000).
[18] M. G. Haines, P. D. LePell, C. A. Coverdale, B. Jones, C. Deeney, and J. P. Apruzese, Phys. Rev. Lett. **96**, 075003 (2006).
[19] J. P. Chittenden, S. V. Lebedev, C. A. Jennings, S. N. Bland, and A. Ciardi, Plasma Phys. Controlled Fusion **46**, B457 (2004).
[20] P. G. Burkhalter, C. M. Dozier, and D. J. Nagel, Phys. Rev. A **15**, 700 (1977).
[21] N. R. Pereira and J. Davis, J. Appl. Phys. **64**, R1 (1988).
[22] S. A. Pikuz, T. A. Shelkovenko, D. B. Sinars, J. B. Greenly, Y. S. Dimant, and D. A. Hammer, Phys. Rev. Lett. **83**, 4313 (1999).
[23] D. B. Sinars, R. D. McBride, S. A. Pikuz, T. A. Shelkovenko, D. F. Wenger, M. E. Cuneo, E. P. Yu, J. P. Chittenden, E. C. Harding, S. B. Hansen, B. P. Peyton, D. J. Ampleford, and C. A. Jennings, Phys. Rev. Lett. **109**, 155002 (2012).
[24] V. V. Ivanov, G. S. Sarkisov, P. J. Laca, V. I. Sotnikov, V. L. Kantsyrev, B. M. Jones, C. A. Coverdale, P. D. LePell, C. Deeney, K. W. Struve, A. L. Astanovitskiy, D. A. Fedin, B. Le Galloudec, V. Nalajala, I. Shrestha, and T. E. Cowan, IEEE Trans. Plasma Sci. **34**, 2247 (2006).
[25] G. E. Sarkisov, A. S. Shikanov, B. Etlicher, S. Attelan, C. Rouille, and V. V. Yan'kov, JETP **81**, 743 (1995).
[26] M. Tatarakis, R. Aliaga-Rossel, A. E. Dangor, and M. G. Haines, Phys. Plasmas **5**, 682 (1998).
[27] B. A. Trubnikov, Sov. J. Plasma Phys. **12**, 271 (1986).
[28] P. V. Sasorov, Sov. J. Plasma Phys. **18**, 143 (1992).
[29] G. S. Sarkisov, Instrum. Exp. Tech. **39**, 727 (1996).
[30] H. Hutchinson, *Principles of Plasma Diagnostics* (Cambridge University Press, New York, 1987).
[31] S. V. Lebedev, F. N. Beg, S. N. Bland, J. P. Chittenden, A. E. Dangor, and M. G. Haines, Phys. Plasmas **9**, 2293 (2002).
[32] C. A. Jennings, M. E. Cuneo, E. M. Waisman, D. B. Sinars, D. J. Ampleford, G. R. Bennett, W. A. Stygar, and J. P. Chittenden, Phys. Plasmas **17**, 092703 (2010).
[33] J. P. Apruzese, J. L. Giuliani, J. W. Thornhill, C. A. Coverdale, B. Jones, and D. J. Ampleford, Phys. Plasmas **20**, 022707 (2013).